

First experimental test of a coded-mask gamma camera for proton therapy monitoring

Magdalena Kołodziej^{a,b,*}, Stephan Brons^c, Mikołaj Dubiel^a,
George N. Farah^d, Alexander Fenger^d, Ronja Hetzel^{d,1}, Jonas Kasper^d,
Monika Kercz^{a,b}, Barbara Kołodziej^{a,b,2}, Linn Mielke^d, Gabriel Ostrzołek^a,
Magdalena Rafecas^e, Jorge Roser^e, Katarzyna Rusiecka^{a,*}, Achim Stahl^d,
Vitalii Urbanevych^a, Ming-Liang Wong^{a,3}, Aleksandra Wrońska^a

^a*Marian Smoluchowski Institute of Physics, Jagiellonian University, Kraków, Poland*

^b*Doctoral School of Exact and Natural Sciences, Jagiellonian University, Kraków, Poland*

^c*Heidelberg Ion Therapy Center (HIT), Heidelberg, Germany*

^d*III. Physikalisches Institut B, RWTH Aachen University, Aachen, Germany*

^e*Institute of Medical Engineering, University of Lübeck, Lübeck, Germany*

Abstract

Objective. The objective of the presented study was to evaluate the feasibility of a coded-mask (CM) gamma camera for real-time range verification in proton therapy, addressing the need for a precise and efficient method of treatment monitoring.

Approach. A CM gamma camera prototype was tested in clinical conditions. The setup incorporated a scintillator-based detection system and a structured tungsten collimator. The experiment consisted of the irradiation of PMMA phantom with proton beams of energies ranging from 70.51 to 108.15 MeV. Experimental data were benchmarked against Monte Carlo simulations. The distal falloff position was determined for both experimental data and simulations.

Main results. The tested CM camera achieved a statistical precision of distal falloff position determination of 1.7 mm for 10^8 protons, which is consistent with simulation predictions, despite hardware limitations such as non-functional detector pixels. Simulations indicated that a fully operational setup would further improve the performance of the detector. The system demonstrated rate capability sufficient for clinical proton beam intensities and maintained performance without significant dead time.

Significance. This study validates the potential of the CM gamma camera for real-time proton therapy monitoring. The technology promises to enhance treatment accuracy and patient safety, offering a competitive alternative to existing approaches such as single-slit and multi-slit systems.

Keywords: coded mask, prompt-gamma imaging, proton therapy, range verification

*Corresponding authors. E-mail addresses: mkolodziej@doctoral.uj.edu.pl (Magdalena Kołodziej), katarzyna.rusiecka@uj.edu.pl (Katarzyna Rusiecka).

¹Present address: Biophysics Department, GSI Helmholtzzentrum für Schwerionenforschung GmbH, Darmstadt, Germany.

²Present address: Medical University of Gdańsk, Gdańsk, Poland

³Present address: Department of Physics, University of Liverpool, Liverpool, UK.

1. Introduction

Proton therapy has become a well-established radiotherapy modality with more than 121 therapy centres currently operational and 30 under construction [1]. Irradiation with proton or heavy ion beams offers an advantageous dose deposition pattern and improved treatment conformity. However, large irradiation margins due to uncertainties in treatment planning, patient positioning, and physiological changes are still among the biggest problems for proton therapy, compromising treatment safety. The development of a method for online monitoring of proton therapy would allow for the reduction of the irradiation margins and thus improve the safety and quality of treatment. The need for such methods was one of the highlights of the report published by the Nuclear Physics European Collaboration Committee in 2014 [2].

Most approaches to real-time monitoring of proton therapy exploit by-products of patient irradiation, one of which is prompt-gamma (PG) radiation. In 2006 it was experimentally proven that there is a correlation between the PG radiation characteristics and the position of the Bragg peak [3]. Since then, PG emission during proton therapy has been extensively studied [4–6]. Several research groups have proposed detectors to determine the proton range or even the dose distribution based on the characteristics of PG radiation, such as timing, spatial distribution, and spectral characteristics. A recent review article by M. Pinto presents a comprehensive summary of the current status of PG based methods of proton therapy monitoring and challenges in the field [7].

Many of the proposed detection setups incorporate passive collimation in various forms. The detection system featuring a knife-edge slit (KES) collimator developed by Richter et al. [8] was the first one to be tested in clinical conditions and proven to provide control of inter-fractional range changes with a precision of about 2 mm. In the second generation of this setup, the detector was mounted on a dedicated support frame, which was docked at a fixed position under the therapeutic table during patient irradiation. Systematic quantitative studies of the introduced improvements yielded an overall uncertainty of range prediction validation of about 1 mm (2σ) [9]. The group recently reported that they achieved a reduction in irradiation margins from 7 mm to 3 mm in patients with prostate cancer using their second-generation KES camera [10]. The group of Xie et al. also tested a KES detection system and proved its feasibility in clinical conditions in pencil beam scanning mode [11].

Another type of detection system which is considered for online range verification in proton therapy consists of the multi-parallel slit (MPS) collimator. Compared to KES, it ensures a larger number of registered photons and offers larger field of view (FOV). MPS systems were tested by means of Monte Carlo simulations [12] as well as in experiments [13]. However, no superiority to the KES systems was demonstrated at the time. The Lyon group has continued analytical modelling and Monte Carlo simulations of the two types of setups [14]. A recent article from Ku et al. reports on a MPS gamma camera that was tested under clinical conditions in spot-scanning mode. The group achieved precision ranging from 2.2 mm to 3.7 mm in range measurements for 10^8 protons, depending on the beam energy. The group is planning to continue their studies with antropomorphic phantoms and patients [15].

Ready et al. proposed a variation of a MPS, featuring many knife-edge-shaped slits [16, 17]. The range retrieval precision achieved was 1 mm (2σ); however, the tests were conducted with a beam energy of 50 MeV, which is well below the clinically applicable energy range. Unfortunately, the studies of that group were discontinued. However, another team has adopted the concept and extended it to a dual-head configuration, enabling 3D imaging. The feasibility of using this setup for online range monitoring in proton therapy was demonstrated through simulations, with a position resolution better than 2 mm across the whole FOV. The group is currently developing a prototype setup to verify their simulation results [18].

Yet another approach to passive collimation is a coded-mask (CM) collimator. The coded mask (CM) is an extension of the well-known pinhole camera concept. In contrast to a pinhole camera, in CM imaging the detector is shielded with a collimator consisting of many holes forming a specific pattern [19]. When irradiated, the collimator casts a shadow on the detector surface. Depending on the position of the radiation source in FOV, the shadow is shifted. Knowing the distribution of hits recorded in the detector and the pattern of the mask, it is possible to reconstruct a 2D image of the radioactive source distribution. Using a CM collimator can be beneficial since even as many as half the pixels can be transparent to radiation, improving detection efficiency. At the same time, a mask pattern can be optimised such that the image resolution and signal-to-noise ratio (SNR) are also improved [20, 21]. A popular choice in CM imaging are modified uniformly redundant array (MURA) mask patterns [21].

CM imaging was originally developed for astrophysics and was used to observe distant gamma-ray sources [22, 23]. Nowadays, the application of CM imaging has broadened and includes localisation of radioactive materials e.g. in nuclear safety and security. With some adaptations of the CM detector, it is also possible to localise sources of neutrons of various energies, which is in particular of interest to those fields [19]. However, it needs to be noted that all of the listed applications entail far-field imaging, rather than near-field, which is the subject of proton therapy monitoring. A setup featuring a pixelated detector and CM with MURA pattern proposed for proton therapy monitoring was studied via Monte Carlo simulations by Sun et al. [24]. The authors reported an accuracy of range determination better than 0.8 mm. However, this result was obtained for 10^{10} impinging protons, which is two orders of magnitude more than is usually applied for a single distal irradiation spot.

The study presented in this article is a continuation of the experiments previously conducted by our group with small-scale prototypes of the CM camera and point-like radioactive sources [25]. In that work, we proved that the CM technique can be successfully applied to the near-field imaging of gamma sources. We have also presented the results of Monte Carlo simulations of the full-scale setup featuring coded masks with a realistic source distribution resembling the conditions of proton therapy. At the statistics of 10^8 impinging protons and in the beam energy range 85.9–107.9 MeV, we obtained the mean precision of beam range estimation of 0.72 mm (1σ).

The promising results of the pilot study led us to construct the full-scale CM detector. The experimental results obtained with the latter are the subject of this report. In the experimental test, the detector was used to detect range shifts in the phantom irradiated with proton beams of various energies. The experiments were carried out at the Heidelberger Ionenstrahl-Therapiezentrum

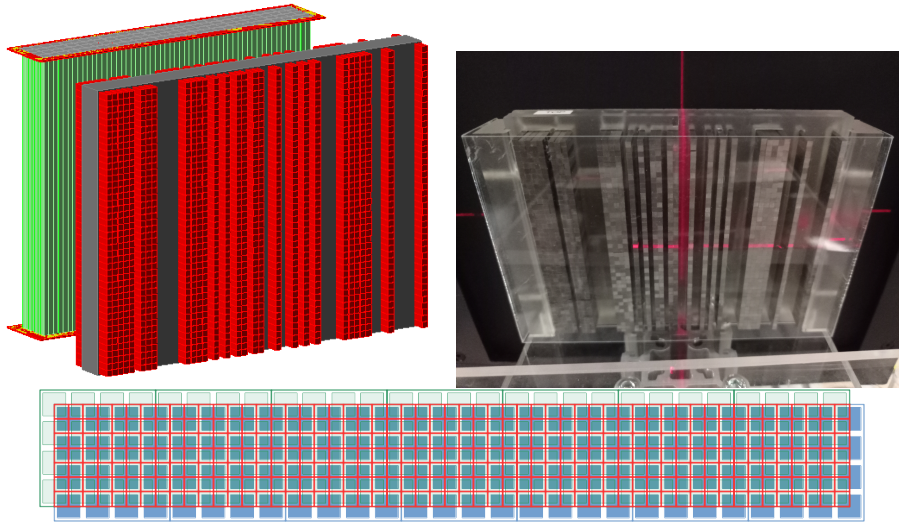


Figure 1: Top left: a schematic of the detector setup: a stack of scintillation fibers (green) with dual top+bottom readout, and a structured collimator made of tungsten rods (red). Top right: collimator - real photo. Bottom: fiber and silicon photomultiplier (SiPM) geometrical arrangement (top view). Red squares represent the fibers, blue and green boxes represent bottom and top SiPMs, respectively.

(HIT). The coded mask pattern used and the overall performance of the sensitive detection part allowed for 1D imaging. In the following, we benchmark the obtained experimental results with Monte Carlo simulations. Furthermore, the simulation results show promising directions for further enhancement of the studied detector performance.

The CM camera described in the following article was developed under the **Silicon Photomultiplier and Scintillating Fiber based Compton Camera (SiFi-CC)** project [26]. The goal of the SiFi-CC collaboration is to construct a novel dual-modality setup for the online monitoring of proton therapy. One of the proposed detection modalities is a Compton camera [27], and the other is a CM camera. Both modalities are being developed in synergy, since they share most of their hardware, such as the sensitive material, front-end electronics (FEE), and data acquisition (DAQ) system. After the necessary upgrade, the detector described in this article will serve in the future as a scatterer module of the full Compton camera proposed by the SiFi-CC group.

2. Materials and methods

2.1. Detection setup

The investigated detection setup was of a CM camera type. The following sections detail its components. The selection of materials and the overall design were based on our earlier studies [25, 28].

2.1.1. Sensitive part - scintillator

The sensitive part was composed of elongated segments (termed *fibers* in this work) of dimensions $(1.94 \times 1.94 \times 100)$ mm³, made of LYSO:Ce,Ca scintillation crystals. This material was chosen for its high effective atomic number

and density, in order to enhance gamma detection efficiency. The fibers were arranged into an array of 7 layers, each layer comprising 55 fibers. Aluminium foil was used as optical insulation between the fibers to prevent optical crosstalk, resulting in an overall fiber pitch of the module of 2 mm. Both the scintillating material and the fiber wrapping material were chosen based on the extensive study [28, 29]. The module was manufactured by Taiwan Applied Crystal [30].

2.1.2. Front-end electronics and data acquisition system

The fiber stack was read out on two opposed sides by SiPMs, as depicted in Fig. 1. 4×4 arrays of the AFBR-S4N44P164M model from Broadcom [31] were selected, as they had one of the highest photon detection efficiencies (68 %) on the market at the time. Moreover, their spectral sensitivity matched well with the LYSO:Ce,Ca emission spectrum. The arrays were housed on custom printed circuit boards (PCBs) which also provided the hardware interface to the FEE. The SiPM form factor of the arrays was 4 mm, i.e. two times larger than that of the fibers in linear dimensions. This means that each SiPM collected light from four fibers. To facilitate identification of hit fibers in a way similar to that described in [32], the top and bottom SiPM boards were not mounted in a mirror configuration, but one was displaced diagonally with respect to the other by half of the SiPM pitch, as shown in the bottom panel of Fig. 1. This reduced the number of required readout channels from 770 assuming the one-to-one fiber-SiPM coupling, to 224 with four-to-one coupling scheme.

Due to an incorrect method of soldering the SiPMs to PCB boards, some of them lost the electrical connection and were thus unusable during the experiment, causing acceptance gaps. Data analysis will exclude these non-working SiPMs and associated fibers. Henceforth, we refer to them as *dead pixels*.

Fibers were coupled to SiPMs using a structured optical interface in the form of stainless steel, 0.5 mm-thick rasters with window patterns that matched those of the SiPM active areas. The function of the raster was to restrict the sensitivity of each SiPM to the fibers that directly faced it. The windows were filled with Elastosil RT 604 silicone rubber [33] to ensure good light transmission.

SiPM signals were further processed to extract the time and charge information in the TOFPET2c ASICs [34] being parts of the integrated, off-the-shelf FEE and DAQ system delivered by the PETSYS company [35]. The system offers a possibility to trigger on events exhibiting a coincidence between two groups of channels, e.g. top and bottom SiPMs in that case. The used combination of PCIe with 3 SFP+ optical/copper connectors can transmit data up to 6.6 Gbit/s. The selection of the FEE+DAQ system was based on an extensive comparative study [36]. The coincidence time window of the DAQ was set to 15 ns and the QDC integration time was 290 ns.

The masses of the detection module and the DAQ setup amounted to 1.6 kg and 1.4 kg, respectively. The light-tight box and the power supply are not included here.

2.1.3. Mask

Imaging experiments were performed using a collimator of the type of a MURA pattern. More specifically, we used a 476-rank 1D mask clipped to the central 57 pixels horizontally, and the pattern repeated over the 45 vertical pixel rows. This collimator is a slightly enlarged version of the one presented in the simulation study of [25] (51 horizontal pixels). The mask construction, as shown

in the right panel of Fig. 1 was based on a 3D-printed structured raster made of Phrozen Aqua Resin Clear, with pockets allowing to insert tungsten rods where filled pixels were foreseen. The rasters had a total thickness of 13 mm and the pockets to insert the rods were 10 mm deep. The mask pixel size was 2.25 mm, the precision of the rods manufacturing was 0.05 mm, and the thickness of the attenuating parts (i.e., the length of the rods) was 20 mm. The linear attenuation coefficient of tungsten amounts to 0.784/cm [37], i.e. 79% of 4.4 MeV gammas are stopped in the mask thickness. A cover made of 0.7 mm thick poly(methyl methacrylate) (PMMA) preventing the rods from falling out was attached to the raster. The total mass of that structured collimator amounted to 3 kg.

2.2. Experiment

2.2.1. Conditions at HIT

Measurements were performed in the experimental room of HIT. The facility offers various ion beam species, of which we exploited protons only. Importantly, the experimental room is equipped with a beam delivery system and a beam nozzle identical to those in the therapy rooms, which allows tests in truly clinical conditions. The machine offers predefined energy and intensity steps as well as several selectable lateral beam widths. Almost all measurements were carried out at the smallest beam width (ranging between 14.5 mm and 22.5 mm in the tested energy range) and the maximum available beam intensity step of 3.2×10^9 protons/s, although several measurements at lower beam intensity were taken for rate capability studies.

2.2.2. Radioactive source

For the auxiliary measurements described in the following points, a $^{68}\text{Ge}/^{68}\text{Ga}$ radioactive source was used. The source had a cylindrical shape of 192 mm length and 3.2 mm outer diameter, while the activity occupied the central part: 184 mm in length and 1.6 mm in diameter. The source decays via β^+ decay, but the shielding is penetrated only by the annihilation gamma quanta, with a small contribution of 1077 keV gammas. At the time of measurement, the source activity was 10.7 MBq.

2.2.3. Energy- and y -position calibration

The light collection on the SiPMs depends on the position of the interaction along the fiber. This fact can be exploited to reconstruct the y -position based on the ratio of signals from both sides of the detector. However, this also implies that the energy calibration is y -dependent. Therefore, a series of calibration measurements was taken. In each of them, the source (described in Section 2.2.2) was placed horizontally, i.e. along the x -axis, at different, known positions along the scintillating fibers. An additional reference detector, in the form of a horizontally oriented LYSO:Ce fiber with dual SiPM readout, was used in coincidence with the main detection module to constrain the direction of the gammas interacting with the latter, and thus their interaction position, taking advantage of the colinearity of a gamma pair emitted in a single act of annihilation. This principle is known as electronic collimation [28, 38]. The AND signal of the two reference detector ends served as the DAQ trigger. The vertical position of the source and reference detector was controlled remotely.

The use of the electronic collimator instead of a passive one ensured better source positioning with the irradiated length of the detector defined by the source - reference detector distance and the source - module distance. The performed position scan consisted of nine 15-minute long measurements taken at 10 mm intervals along the scintillating fibers, starting 10 mm away from one end of the detector and finishing 10 mm away from the opposite end.

2.2.4. Experimental setup for imaging

The setup was arranged as shown in Fig. 2. A PMMA ($50 \times 50 \times 90$) mm³ phantom with density of 1.19 g/cm³ was used as a target. The setup components were aligned with respect to the beam axis using the laser markers available in the experimental room, defining the beam axis and the isocentre. The longest axis of the phantom was aligned with the beam axis, the mask was located at a distance of 170 mm from it (distance to the mask centre), and the mask-detector distance was 63 mm (centre-to-centre). Those distances are as close to the optimum found in [25] as was possible, given the constraints resulting from the presence of the light-tight box and components of the support structures. The setup geometry results in the fully coded field of view (FCFOV) of (176 × 100) mm², though in the following we restricted the analysis to FOV of (140 × 100) mm². As seen in Fig. 2, the box housing the detector offered enough free space for convenient detector manipulation that takes place frequently in the prototyping phase. The DAQ electronics were located in a separate housing to reduce unwanted heat dissipation in the direct vicinity of the detector.

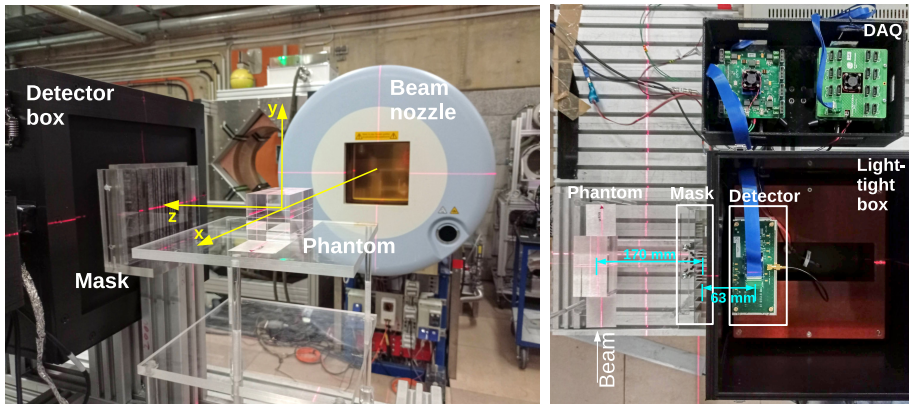


Figure 2: Detection setup in imaging experiments: perspective view (left) and top view (right).

2.2.5. Proton beam measurements

We performed a series of measurements with different beam energies to test the beam range-shift retrieval capabilities of the setup. The corresponding beam energies, beam ranges as calculated using the PSTAR tool [39], and beam lateral positions are presented in Table 1 along with the spot symbols referring to Fig. 3. The numbers of protons used for a single irradiation are also specified. The default number was 10^{10} protons, although for three spot locations ten times larger data samples were also recorded. Those measurements are referred to as primed (e.g. S3').

Table 1: Energies and ranges (calculated using PSTAR [39]) of the beam used in the experiment. Spot symbols refer to Fig. 3.

Spot symbol	Beam energy [MeV]	Range [mm]	Lateral position (z, y) [mm]	N protons
S1	70.51	36.63	(0,0)	10^{10}
S2(S2')	81.20	45.88	(0,0)	10^{10} (10^{11})
S3(S3')	86.14	50.99	(0,0)	10^{10} (10^{11})
S4(S4')	90.86	56.09	(0,0)	10^{10} (10^{11})
S4a			(0,10)	10^{10}
S4b			(0,-10)	
S4c			(-10,0)	
S4d			(10,0)	
S5	95.40	61.19	(0,0)	10^{10}
S6	99.78	66.27	(0,0)	10^{10}
S7	108.15	76.46	(0,0)	10^{10}

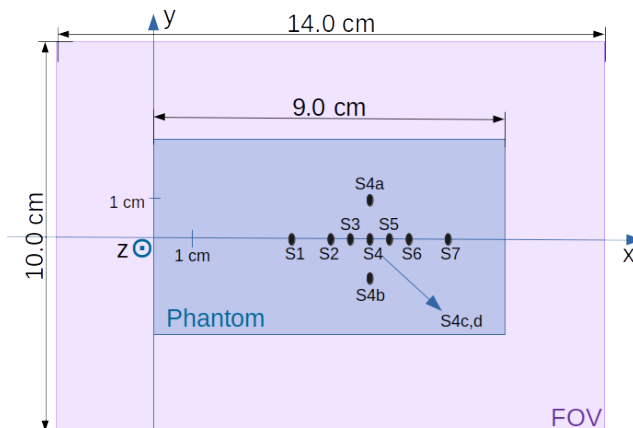


Figure 3: Location of the irradiated spots in the phantom overlaid with the camera FOV - side view. Beam direction is $+\hat{x}$. For depth S4, data for four additional spots differing in lateral coordinates were taken. They are denoted with an additional character (e.g. S4c). Origin of the coordinate system, located in the phantom centre, is shown displaced for the sake of picture clarity.

2.2.6. Efficiency and background studies

The registered spatial distribution of PG interaction points can be distorted in two ways: by a non-uniform detector efficiency, as well as a background contribution from intrinsic lutetium activity in LYSO:Ce,Ca . To quantify both effects, additional measurements were performed. LYSO:Ce,Ca background was investigated in a dedicated measurement, with both the collimator and the radioactive source removed. For the efficiency studies, a measurement with the linear radioactive source and in the absence of the collimator was recorded. The source was oriented parallel to the beam axis, at a distance of 233 mm from the detector centre. Recorded data were background-subtracted and compared with

the corresponding ones from simulations (see Section 2.3.2 and Section 3.2) to calculate the detection efficiency maps. Both the efficiency and the background measurements lasted 5 min.

2.3. Simulations

To simulate the reactions of the protons inside the target, we used the 10.4.2 version of the Geant4 package [40] and the QGSP_BIC_HP_EMZ physics list [41]. This combination was found to deliver results closest to experimental ones as regards prompt gamma (PG) production [42]. Additionally, we used the GODDeSS package, which is an extension to Geant4 that manages optical physics in scintillators [43], to build scintillation volumes, and to process optical photons to generate signals in the detector.

2.3.1. Setup response to PG radiation

To assess the performance of the CM setup, we performed Monte Carlo simulations corresponding to the experimental conditions. The simulated setup was identical to the experimental one (see Section 2.2.5). The simulation process was divided into two separate steps:

1. A proton beam interacts with the phantom. Secondary particles are produced and propagated until they leave the target. The corresponding secondary phase-space files are stored.
2. Gamma quanta from phase-space files are used as input for the simulation of interactions of the particles with the detector. The simulation tracks the optical photons generated in the detector fibers until they are registered by SiPMs. Additionally, specific SiPM properties like wavelength-dependent photon detection efficiency, cross talk, dark counts, recharge timing are modeled and taken into account to mimic the measured detector signals. The output files contain information about the PGs that triggered the detector, the data registered by SiPMs, as well as Monte Carlo truth about the hits in the fibers.

2.3.2. Reference for efficiency studies

One of the components needed to obtain an efficiency map is a simulation of the interaction probabilities in the detector. The simulated setup was identical to the one in the efficiency measurement described in Section 2.2.6. The number of simulated gammas from phase space files was 4×10^8 and the polar angle of the emitted gammas was restricted to $\theta < 35^\circ$ to speed up the simulations. At the same time, this limit of the θ angle ensured that the gammas emitted from every part of the source which were within the detector acceptance were represented in the data sample.

2.3.3. System matrix

To reconstruct PG depth profiles based on the CM camera data we used maximum-likelihood expectation maximisation (MLEM) algorithm, which requires information about the probability of registering a particle emitted from a specific position in the source plane in a specific part of the detector. This information is represented by the so-called system matrix (SM). The procedure is described in more detail in Section 2.5. The system matrix was determined using the simulations of the CM setup response. Here, the detector response

to point-like sources of PGs is of interest. Thus, instead of using the first step of the simulation framework, we used the General Particle Source. The FOV of 140 mm was divided into 100 bins along the x -axis and a single bin in y centred in the middle of the detector height. For each individual simulation, a gamma source was placed at the centre of the corresponding bin, and 6.5×10^6 gamma quanta were simulated. Each time, the angle of emission was restricted to $\theta < 50^\circ$, which was chosen to be large enough to cover the entire mask from each source position. The energy spectrum of the simulated gamma particles was obtained from the spot S4 phase space file.

2.4. Analysis chain

The complete data set for the evaluation of the performance of the CM gamma camera contained: i) data for all beam spots in Fig. 3; ii) reference measurement without the CM collimator with a linear $^{68}\text{Ge}/^{68}\text{Ga}$ source for efficiency determination, and iii) background, measured at least 30 minutes after the last beam run, to eliminate the background component coming from activation of the setup parts by the beam. The data processing scheme is summarised in Fig. 4.

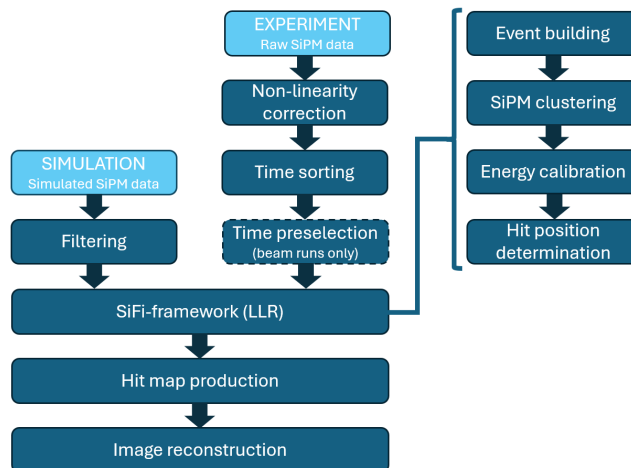


Figure 4: The processing scheme of the experimental and simulated data.

The raw data collected in the experiment were saved in binary format. A single data entry was a set consisting of the ID of SiPM that registered a signal, the time of the signal registration, and the signal charge (QDC value) registered. Data were first corrected for a DAQ-specific nonlinearity effect [44] and saved as ROOT trees [45]. Then, they were sorted by time. Measurements with the beam were additionally divided into beam spill and inter-spill background parts. The trees processed in this way were then input into low-level reconstruction (LLR), which consisted of event building, clustering, and reconstruction of hit positions and energy deposits in the detector. LLR was performed with custom software, the SiFi-framework [46].

We performed LLR on the simulation results in the same way we analysed the experimental data. In the case of the simulations, the data were already time-sorted and there was no need for DAQ-specific non-linearity correction,

but an extra step of filtering out inactive SiPMs was necessary. After that, the processing scheme was identical.

2.4.1. Data preselection: signal and background subsets

The measurements with the beam needed an additional preprocessing step: time preselection. The event time distribution of an example run S4 presented in Fig. 5 reflects the synchrotron beam time structure. One can see a region with increased counts corresponding to the beam spill, and an almost constant background. The data for each beam run were divided into spill and background subsets. The hit maps for these subsets are presented in Fig. 7 (a) and (b), respectively; their energy spectra are plotted in Fig. 6. The background is considered during the image reconstruction procedure (see Section 2.5).

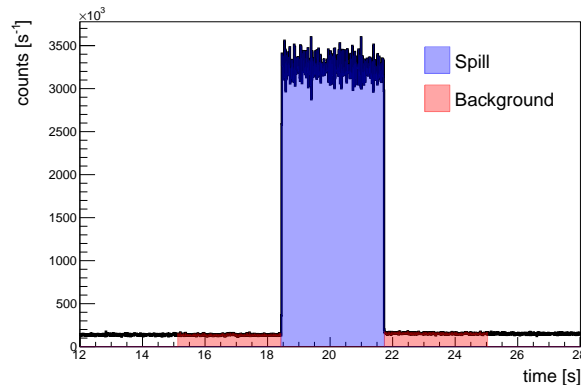


Figure 5: Time structure of the proton beam, with separation to the spill (blue) and the background (pink) parts.

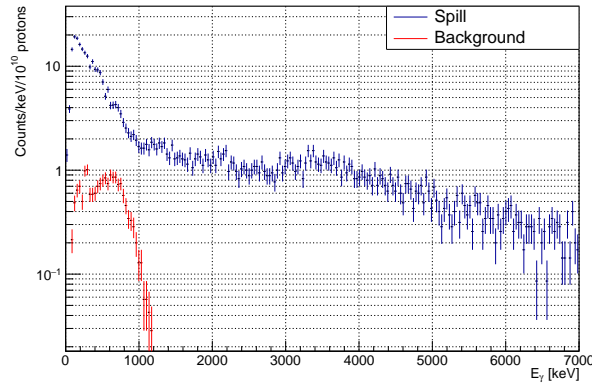


Figure 6: Comparison of gamma energy spectra for spills and background for beam spot S4. The background was scaled to its expected content during the spill.

2.4.2. Event building and clustering

The events were built out of single entries, based on time information: any entry that belonged to a fixed time window of 15 ns was assigned to the same

event. The length of the window was inferred from a histogram of time difference between subsequent entries.

Within the events, SiPM clusters were found, separately for the top and bottom detector side. Then, for each pair of clusters, common fibers were found. We ensured that the fibers within those cluster pairs were grouped together, i.e., any fiber neighbored at least one other fiber. The events were classified as belonging to one of five categories, depending on the number of SiPM clusters; the abundance of the event types for run S4 (spill) is given in brackets:

1. unique cluster, unique fiber: there is only one common fiber between the top and the bottom clusters (40.86 %);
2. unique cluster, multiple fiber: there is one top cluster and one bottom cluster, but more than one common fiber coupled to them (49.28 %);
3. top semi-unique cluster: two clusters on the bottom side, but one cluster on the top (5.58 %);
4. bottom semi-unique cluster: two clusters on the top side, but one cluster on the bottom (4.07 %);
5. ambiguous cluster: more than one cluster on both top and bottom sides (0.21 %).

2.4.3. Reconstruction of hit position and energy deposit

The goal of LLR in our case was to obtain the hit positions in x and z dimensions for each event, along with the hit time and the energy deposit.

The cluster hit time for all event types was the time of the first entry in the corresponding pair of SiPM clusters.

Each of the event categories listed in Section 2.4.2 was handled differently as regards to the hit position and energy determination in LLR:

- The hit position for type-1 events was simply the position of the only fiber, and the energy deposit was the summed deposition in the top and bottom clusters.
- For type-2 events, we defined the hit position along the layer (x) as the mean of active fiber IDs, weighted by the fiber energy deposit (which was the geometric average of energy deposits in SiPMs coupled to a single fiber). The hit position value was rounded to the ID of the closest fiber. The hit position across the layers (z) was defined as the frontmost detector layer with an active fiber. Fiber positions were expressed by f and l , i.e. the fiber number in the layer and the layer number, respectively. The energy deposit for type-2 events was determined as $\sqrt{E_T E_B}$, where E_T , E_B are summed energy deposits of all SiPMs forming the top (T) or bottom (B) cluster.
- Type-3 and type-4 events: prior to the hit position determination, one needs to separate the energy value of the merged cluster into two, according to the ratio of energies in clusters on the other side. The rest of the processing chain was the same as for type-2 events.
- Type-5 events were excluded from further analysis.

Prior to the energy assignment, the QDC values for all SiPMs were calibrated with the use of an auxiliary measurement with a $^{68}\text{Ge}/^{68}\text{Ga}$ radioactive source

allowing one to find a scaling factor based on the 511 keV peak position. The scaling was then applied in LLR, to translate the QDC values to energy in keV.

2.4.4. Data representation: hit maps

As a next step, from the lists of fiber hits, we created maps of hits, as shown in Fig. 7. One pixel in such a map corresponds to one fiber, and each bin is filled with the number of hits registered in the corresponding fiber. The maps have dimensions of 7×55 pixels, which corresponds to spatial arrangement of fibers. We constructed hit maps with various lower energy thresholds (0, 0.5, 1, 1.5 MeV), and a common upper threshold of 7 MeV. Such hit maps were the input for image reconstruction, described in Section 2.5.

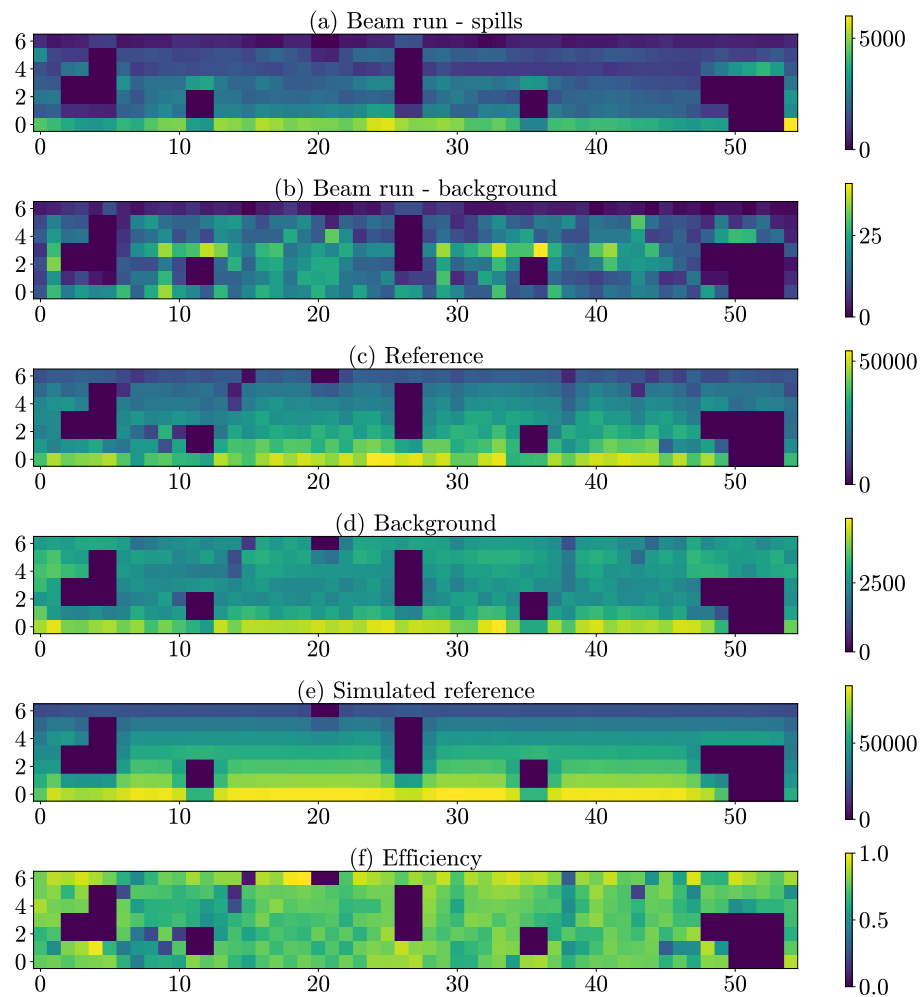


Figure 7: Components of the image reconstruction, presented in the form of hit maps. On the hit map, the horizontal axis corresponds to the fiber number in the layer (f), with the layer number (l) in the vertical axis. a) spill part for S4; (b) background part for S4; (c)-(e) components of efficiency calculation: reference measurement, background and simulated reference, respectively; (f) efficiency calculated from components (c)-(e), as described in Section 3.2.

2.5. Image reconstruction

2.5.1. Implementation of MLEM algorithm

To reconstruct the PG depth profiles⁴ from the measured data, the MLEM [47,48] was implemented according to the following formula:

$$\mathbf{f}^{(k+1)} = \frac{\mathbf{f}^{(k)}}{\mathbf{S}} \mathbf{A}^T \frac{\mathbf{y}}{\mathbf{A}\mathbf{f}^{(k)} + \mathbf{b}}, \quad (1)$$

where the vectors $\mathbf{f}^{(k)}$ and $\mathbf{f}^{(k+1)}$ represent the reconstructed PG depth profiles after iterations k and $k + 1$, respectively; the element $f_j^{(k)}$ is thus the reconstructed number of emitted prompt gammas at the depth bin j , with $j \in \{1, 2 \dots J\}$ and $J = 100$; the vector \mathbf{y} corresponds to the histogrammed measured data (hit maps), while \mathbf{b} is the estimated background; both vectors consist of 303 elements, i.e., the number of all detector pixels (385) minus the dead ones. The dead pixels were consistently removed from all other components of the MLEM formula. The background elements b_i is a sum of what the detector pixel i registers 3 s before and 3 s after the beam spill (see Fig. 5). The background was normalised to match the spill duration.

\mathbf{A} denotes the system matrix, whose elements a_{ij} represent the probability that a PG emitted from the source bin j is registered by the detector pixel i . First, we calculate \tilde{a}_{ij} , i.e., the ideal system matrix for uniform efficiency, using the simulation described in Section 2.3.3: the recorded data are processed with the analysis chain described in Section 2.4), and for each source position j , the number of the registered gammas in detector pixel i are computed. To convert this value into a probability, these values are divided by the number of gammas that would be emitted into the full solid angle in the performed simulation. The system matrix is presented in Fig. 8.

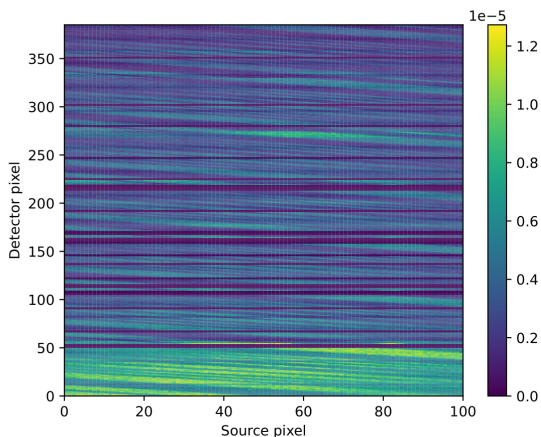


Figure 8: The system matrix - constructed from hits with energy deposits 1–7 MeV.

⁴In the following, we term the PG depth profiles also *images*, even though they are one-dimensional, for the method they are obtained (image reconstruction algorithm).

Differences in the detection efficiency between detectors pixels were also modeled into \mathbf{A} . Efficiency variations are usually caused by hardware imperfections, such as flaws in the fibers, uneven or dirty coupling pads, machining of the SiPMs etc. To correct for these effects, two additional measurements of detector response to a linear $^{68}\text{Ge}/^{68}\text{Ga}$ source (R) and to the pure LYSO:Ce,Ca background (B) were performed (see Section 2.2.6), along with the corresponding simulation of the detector response to the radioactive source (SR), see Section 2.3.2. For the detector element i , the efficiency correction factor was calculated as $\epsilon_i = (R_i - B_i)/SR_i$. Next, the system matrix elements were calculated as $a_{ij} = \epsilon_i \tilde{a}_{ij}$.

The elements of the sensitivity \mathbf{S} were calculated as $S_j = \sum_{i=1}^I a_{ij}$.

2.5.2. Determination of distal falloff position

The crucial part of the PG depth profile, reconstructed according to the description in Section 2.5.1, is the distal falloff. The distal fall-off position (DFP) is strongly correlated with the proton range in the tissue [3]. We determined DFP according to the procedure described in [49], by fitting a spline to the falling edge of the gamma profile. The fit range was set between the global maximum of the profile and a minimum further downstream the beam (in our representation: to the right of the maximum). As DFP, we took the x position of the point with half-value between the maximum and the minimum values. This value is subsequently compared with the proton range calculated using PSTAR [39] for PMMA and the proton beam energies used.

2.5.3. MLEM performance metrics

To assess the image reconstruction performance, we defined three metrics based on the relation between the reconstructed DFP and the calculated proton range PR:

- Pearson correlation coefficient;
- root mean squared error (RMSE):

$$\text{RMSE} = \sqrt{\frac{\sum_{i,j,i \neq j} (\Delta_{\text{PR}} - \Delta_{\text{DFP}})^2}{2n}}, \quad (2)$$

$$\Delta_{\text{PR}} = \text{PR}_i - \text{PR}_j,$$

$$\Delta_{\text{DFP}} = \text{DFP}_i - \text{DFP}_j,$$

where $n = 21$ is the number of all pairs of measurements and $i, j \in [1, 7]$ denote the number of beam spots. Δ denotes the difference between two distal falloff positions (Δ_{DFP}) or two proton ranges (Δ_{PR}). The additional factor of 2 in the denominator reflects the fact that RMSE is calculated based on two experimental points;

- slope of the linear fit to DFPs versus proton range for all spots.

In the optimisation process, we aimed for the correlation coefficient to be as high as possible, the RMSE as low as possible, and the slope preferably as close to one as possible.

2.5.4. Optimisation of image reconstruction parameters

Using the metrics described above, the following reconstruction parameters were optimised:

- number of iterations,
- threshold of energy deposit in hit maps,
- PG depth profile smoothing method,
- excluded detector regions,
- classes of events included.

Using the performance metrics, the reconstruction was optimised and the best parameters were found.

2.5.5. Analysis of statistical precision

Data sets for all beam spots were randomly rearranged into 100 smaller subsets with the bootstrapping method. The sizes of the subsets corresponded to 2×10^9 , 1×10^9 , 4×10^8 , 2×10^8 and 1×10^8 protons on target. Then, the reconstruction with optimal parameters was performed on the subsets and, based on the distribution of the reconstructed DFPs, the statistical precision of the DFP determination was assessed.

3. Results

3.1. Calibration results

The gamma energy spectra obtained in the calibration measurements for each fiber in the detector, featuring an annihilation peak, were later used for the calibration procedure. The calibration procedure developed by us in the single fiber tests [29] and the tests with detector prototypes [28] was applied. As a first step, the parameters of the exponential light attenuation model with light reflection (ELAR) were fitted to the experimental data [29]. Then, having QDC values recorded at both fiber ends, the interaction point coordinate along the fibers (y) and the deposited energy can be reconstructed event by event. The obtained distributions yield the position- and energy resolution of the detector. In the presented experiment, the mean energy resolution was $6.5 \pm 0.5\%$ (1σ) and the mean position resolution was 74 ± 10 mm (FWHM). The resolutions were determined based on the results obtained for about 70% of all fibers (excluding dead pixels and those for which the initial ELAR model fit failed).

3.2. Detection efficiency

Determination of efficiency, as described in Section 2.5, can be followed by analysing panels (c)-(f) of Fig. 7. The distortions in the direct neighbourhood of the dead pixel areas that are the artefacts of the LLR can be clearly seen in the efficiency map (f). After excluding the dead pixels, the relative standard deviation of fiber efficiency yielded 11.39%. The mean efficiency (normalised to the pixel with maximum efficiency) was 0.746(85).

3.3. Rate capability

For beam energies corresponding to spots S4 and S7, three measurements at different intensity steps were performed to study the rate capability of the system. The steps were at 8×10^7 , 6×10^8 , and 3.2×10^9 protons/s. In each case, 10^{10} protons were shot at the phantom, thus - after background subtraction - the same number of incoming PGs was expected for runs at the same beam energy. The integration was performed using histograms of signal timestamps, such as the one in Fig. 5. For each beam energy, the obtained net spill integrals were consistent within uncertainties, i.e. no measurable dead time of FEE+DAQ was observed. At the highest energy and intensity step investigated in the whole experiment, the average count rate per channel was 26.4 kcps, while the limit of deadtimeless operation given in the ASIC manual is 480 kHz [50].

3.4. PG depth profiles from experimental data

The number of entries in the hit maps produced from the beam data for 10^{10} protons increased from 4.7×10^5 for the spot S1 to 8.5×10^5 for spot S7, while the dominating background component, being the intrinsic LYSO:Ce,Ca activity, remained constant. Hence, the background contributions in the spill data were decreasing from 0.50% to 0.30%. Based on those hit maps, we reconstructed the PG depth profiles for different beam spots (see Fig. 3). We checked how well the distal falloff positions for all of the profiles correlate with the calculated proton beam range. Based on this correlation, we assessed the accuracy of our reconstruction procedure. The PG depth profiles for beam spots S1-S7 are presented in Fig. 9 (top panel).

The crucial part of the profile, the distal falloff, is of good quality: its shape is consistent for all beam spots and it contains no major reconstruction artefacts, even though in some profiles changes of steepness can be observed. The rest of the profile, however, presents some features that are unfavourable: although the profiles broaden with increasing depth in the phantom, which is expected, additional wide peaks become visible. This could be due to the Gibbs phenomenon. In addition, it is expected that the rising edge starts at the phantom entry, so that its half-maximum is located close to the phantom border at -45 mm. We observe the rising edge starting deeper in the phantom; it also shifts to the right with increasing beam energy. Finally, in the regions outside of the phantom, there is an increase in relative gamma counts, even though no such increase is expected from physics. These effects are checked against the simulation in Section 3.6.

The distal falloff positions of these profiles are plotted against the calculated proton ranges in Fig. 9 (bottom panel). The reconstruction parameters were optimised according to the scheme described in Section 2.5.3, yielding the following values:

- number of iterations: 23;
- lower threshold of energy deposit in hit maps: 1 MeV;
- PG depth profile smoothing with a Gaussian filter, with a kernel standard deviation of 3 pixels;
- excluded detector regions: dead pixels and 3 most lateral columns of pixels on both detector sides;

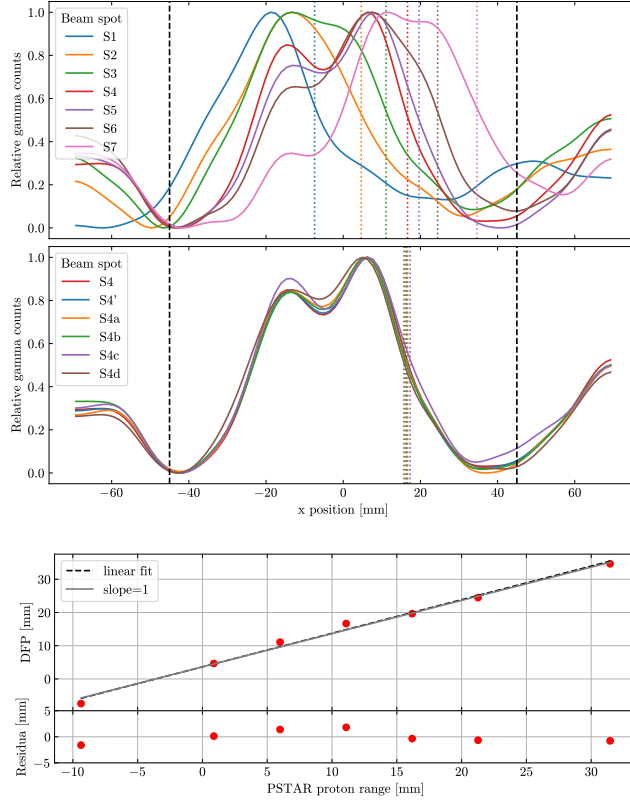


Figure 9: PG depth profiles reconstructed from experimental data, smoothed with Gaussian filter. Top panel: profiles for beam spots S1-S7, vertical dotted lines indicate extracted DFPs, while the dashed lines mark the phantom edges; middle panel: profiles for beam spots S4, S4', S4a-d (same depth in phantom); bottom panel: distal falloff position vs. proton range, with residuals (distances of the data points from the fitted line). The black dashed line is a linear fit to the data, the grey line is a corresponding line with the same intercept as the fit line, but with the slope equal to 1.

- classes of events included: unique and semi-unique.

The RMSE of this set of reconstructions (for 10^{10} protons each) is 1.7 mm. The remaining performance metrics are summarised in Table 2, along with the corresponding data for simulations, which are presented in detail in Section 3.6.

The regions excluded from the analysis were: the dead pixels, the three front (indexed 0-2) and three last (52-54) columns of the detector. The front columns were excluded, because we observed an increased number of counts there due to primary protons from the beam reaching the detector. That was the conclusion drawn based on the spectra of energy deposits in that part of the detector, which extended up to 30 MeV. We excluded the three last columns for symmetry reasons, but also because there was a large fraction of dead pixels there.

The lower hitmap threshold was chosen to be 1 MeV, as it was the most robust, cut out most of the background (see Fig. 6), but also did not significantly reduce the statistics, which would increase statistical fluctuations.

Table 2: Performance metrics used in the image reconstruction. Full simulation is the simulation with all SiPMs active, i.e. without the acceptance gaps.

	Experiment	Simulation	Full simulation
Correlation coeff.	0.996012	0.998072	0.999768
RMSE [mm]	1.7	1.6	0.4
Slope	1.0102(16)	0.94351(68)	0.999981(92)

3.5. Analysis of statistical precision

We performed the reconstruction on smaller size data samples, as described in Section 2.5.5. The results are presented in Fig. 10. There are seven plots for beam spots S1-S7, arranged in ascending beam energy order. The horizontal axis represents the sample size used for image reconstruction, and the vertical axis shows the reconstructed DFP in mm. For each data point (box) in this plot, 100 reconstructions were performed. The plot type is a standard box plot, i.e. the rectangle (box) is the interquartile range (IQR) between the quartiles Q1 and Q3. The line denotes the median. The whiskers extend to the furthest data point that falls into a range of $1.5 \cdot \text{IQR}$, starting from the box edge. Any data point outside the whiskers range is marked with an empty circle.

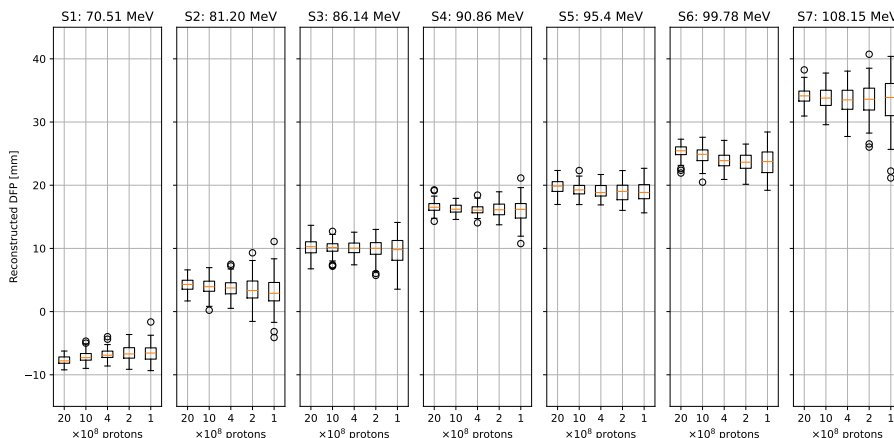


Figure 10: Analysis of statistical precision: median and IQRs of the reconstructed DFPs vs. sample size, for beam spots S1-S7.

For all but the deepest beam spot (S1-S6), the IQR is below 3 mm, even for the smallest sample size (10^8 protons). The deepest spot (S7) has larger IQR, but for the smallest sample size, it is still about 5 mm. The IQR increases with decreasing sample size in most cases; however, some exceptions can be observed, e.g. for S3 the IQR for sample size of 20×10^8 is larger than for 10×10^8 , which is counterintuitive. We suspect this effect could be caused by the use of the bootstrapping method. Moreover, we observe that the median value varies slightly for decreasing sample size, it decreases for beam spots S2 and S6, increases for S1, for the remaining beam spots no clear pattern is observed.

3.6. PG depth profiles from simulation data

To compare the simulation results with the experiment, we reconstructed PG depth profiles from the simulation data. The simulation procedure is detailed in Section 2.3. To ensure consistency with experimental conditions, we disabled the SiPMs that were not operational during the experiment and used the same reconstruction parameters as for the experimental data. Image reconstruction was performed for beam spots S1-S7, and the results are presented in Fig. 11.

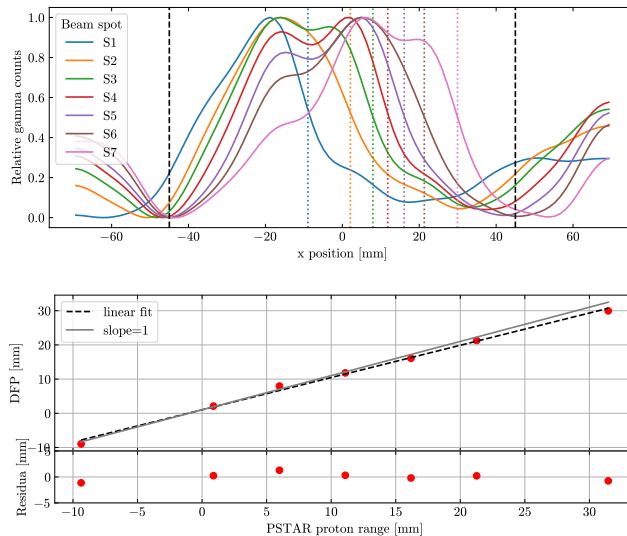


Figure 11: PG depth profiles reconstructed from simulated data, smoothed with Gaussian filter. Top panel: profiles for beam spots S1-S7; bottom panel: distal falloff position vs. proton range, like in Fig. 9.

The simulated PG depth profiles present features similar to the experimental profiles (see Section 3.4).

To evaluate the impact of acceptance gaps on PG profiles, we performed the reconstruction with all SiPMs functioning. The corresponding results, shown in Fig. 12, demonstrate that the artefacts described above are now significantly reduced: the reconstructed gamma intensities in the FOV regions outside of the phantom are low and stable, the rising edge appears earlier and overlaps well with the phantom proximal edge, and the distal falloff shapes are nearly identical for all energies. In this case, the number of iterations was re-optimised and found to be 600, which was higher than for the experimental data. The rest of the reconstruction parameters remained unchanged.

Performance metrics for these reconstructions are presented in Table 2.

4. Discussion

4.1. Experimental and simulated PG depth profiles

A qualitative comparison of PG depth profiles reconstructed from experimental data and from simulation accounting for most of the experimental effects (Figs. 9 and 11, respectively) shows that both sets possess very similar features.

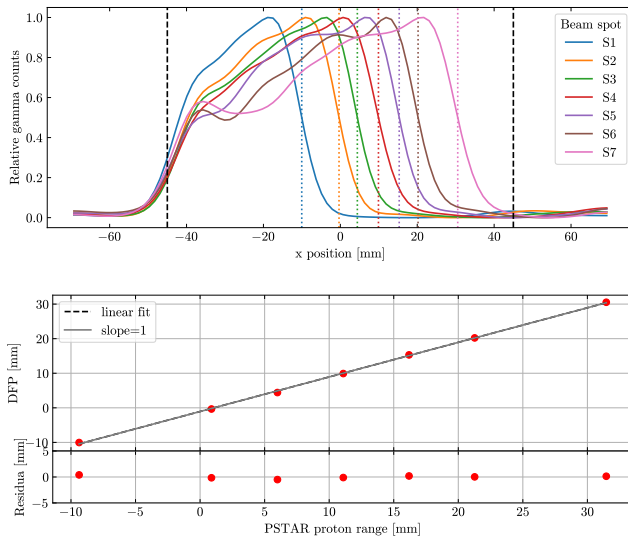


Figure 12: PG depth profiles reconstructed from simulated data without acceptance gaps (non-filtered), smoothed with Gaussian filter. Top panel: profiles for beam spots S1-S7; bottom panel: distal falloff position vs. proton range, like in Fig. 9.

A more detailed, quantitative analysis checking the linearity of the DFP dependence on the proton range also shows that the resulting RMSE values for both sets are almost the same (see Table 2). This gives us confidence that the implemented setup description and the remaining simulation settings in our simulations describe the irradiation experiments accurately and realistically.

The spread of the DFPs extracted for all the spots at the depth of S4, including those with modified lateral beam positions and increased number of impinged protons, was not larger than the achieved DFP precision. Hence, we conclude that the camera is not sensitive to the variation of the beam lateral position within ± 1 cm.

The investigated setup was not free from construction flaws, i.e. non-working SiPMs. This reduces the information available for image reconstruction and introduces artefacts in hit maps. To analyse this effect and assess its impact on the quality of beam range assessment, a data set with a fully operational detector was simulated and analysed. When repeating the process of optimisation of image reconstruction for this data set, we noticed that here, the performance metrics favour higher numbers of iterations, even up to 600, while 23 was the optimum for experimental data. For the latter, the acceptance gaps in the detector introduced artefacts in the PG depth profiles, which were amplified for larger numbers of iterations, deteriorating the reconstruction performance. That was not the case for the full-simulation data, free from acceptance gaps. Consequently, the accuracy of range shift determination measured with RMSE could be improved by a factor of 4 - see Table 2. This remains to be confirmed experimentally, with the upgraded readout PCBs.

4.2. Clinical feasibility

Rate-wise, the setup is ready to operate at clinical beam intensities of a synchrotron-based therapy centre. Moreover, there is still room to safely in-

crease the rates by a factor of 18 without introducing substantial dead time. This makes the setup operational also at a cyclotron-based centre, in which the instantaneous beam intensities are typically ten times larger than at a synchrotron.

The studies of statistical precision in DFP determination presented in Section 2.5.5, translated to the usual metric of standard deviation (1σ) are summarized in Fig. 13. Evidently, the DFP precision excels in the region close to

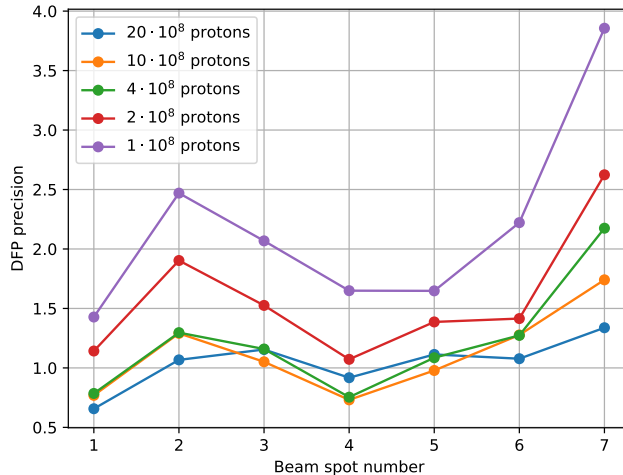


Figure 13: Precision of DFP determination across the FOV for different numbers of protons used in phantom irradiation.

the reference spot S4. The precision is not only a function of the statistics used in image reconstruction, but also of the position in the FOV. The imaging resolution in the most downstream region is about two times worse due to the presence of broader slits in that part of the collimator. Another contribution may come from the neutron background which is expected to be larger at higher beam energies, although the reconstructed profiles do not give a clear supporting evidence.

Our results are the first experimental test of a CM camera for proton therapy monitoring. Other setups, however, have been extensively tested. Table 3 compares the performance of the best solutions currently reported in the literature. For the comparison we have selected data from spot S4, as the one that was most extensively investigated, and the number of protons 10^8 , as it is close to a typical distal spot intensity. As some of the referred publications contain results for multiple beam energies and integrated beam intensities, data for energies and numbers of impinging protons closest to those above have been selected.

Clearly, the KES setups present much more mature solutions than our camera, are integrated with the therapeutic environment and equipped with support structures offering translational and rotational degrees of freedom enabling pre-

⁵The range of precision 0.7-1.3 mm given by us in Table 2 of [25] was incorrect - it corresponded to the precision of range shifts aggregated over all spots in 9 energy layers, not a statistically-driven precision of a single spot.

Table 3: Precision (1σ) of DFP/range estimation by different groups and different prompt-gamma imaging (PGI) approaches. All cases but one (see Comments) are 1D imaging.

Approach	T_p [MeV]	N_p	Precision [mm]	Comment
CM exp. (this work)	90.86	10^8	1.7	ref. position in FOV
CM sim. [25]	85.9–107.9	10^8	0.72	
CM sim. [51]	122.7	10^8	2.1	2D imaging
MPS exp. [15]	99.68	10^8	1.5	
MPS sim. [52]	160	10^8	1.30–1.66	
KES clinical [11]	100–160	10^8	$\sim 2.0^5$	with spot aggregation
KES clinical [9]	160	1.4×10^8	2.0	2 nd generation setup

cise positioning. They have also been incorporated into the clinical workflow. However, when comparing their achieved DFP/range precision achieved per 10^8 -proton spot, without spot aggregation, our solution performs very similarly, or even somewhat better, despite the flaws in hardware. Removal of the latter, according to the simulation results, is expected to significantly improve the setup precision in range determination, even below the level presented by the currently best performing setup: MPS of [15]. The CM gamma camera offers also a larger FOV than KES setups at comparable or smaller material budget.

4.3. Prospects for 2D imaging

As shown in [51] and in our tests with a small-scale prototype [25], the CM setup can also be used for 2D imaging. For this purpose, good position resolution is needed in all dimensions. In the case of the tested setup, even though we intended to test this modality with the current setup, the x and z coordinates of the interaction point are reconstructed based on the identification of responding fibers, while the y coordinate needs to be reconstructed from the top/bottom signal ratio. Even though in the R&D phase the materials of the sensitive part were carefully optimised to achieve the relevant y -position resolution, which was verified in measurements with single fibers and small-scale prototypes, the eventually delivered scintillation module presented a much worse performance in this aspect, see Section 3.1, disabling the 2D imaging option. This, however, will be tested in the future, after the planned reiteration of the construction of the detector sensitive part.

5. Conclusions

The presented study demonstrates the feasibility of the CM gamma camera for proton therapy monitoring, providing a novel approach to PGI with promising experimental results. We tested the scintillating-fiber-based detector with a coded mask collimator in clinical conditions at HIT. In the experiment, a PMMA phantom was irradiated with proton beams of energies ranging from 70.51 MeV to 108.15 MeV and three intensities ranging from 8×10^7 to 3.2×10^9 protons/s. The tested setup achieved a precision in DFP determination of 1.7 mm with 10^8 protons at the beam energy of 90.86 MeV. Obtained gamma depth profiles were benchmarked with the results of Monte Carlo simulations, showing

good agreement. Simulations of the setup without the acceptance gaps (non-filtered) showed that the setup performance can be further improved. In the rate capability studies, we proved that the detector can handle both synchrotron and cyclotron beam intensities without a significant dead time. Comparison with other existing setups of similar characteristics shows that the SiFi-CC CM gamma camera is a competitive solution with the potential to be used in clinical practice. Future plans of the collaboration include the elimination of the acceptance holes and exploration of 2D imaging possibilities.

Acknowledgements

The work presented in this paper was supported by the Polish National Science Centre (grants 2017/26/E/ST2/00618 and 2019/33/N/ST2/02780). The exchange of staff and students between Poland and Germany was possible thanks to the support of the Polish National Agency for Academic Exchange (NAWA) as well as the German Academic Exchange Service (DAAD) (project-ID 57562042). In this context, the project on which this report is based was funded by the German Federal Ministry of Education and Research (BMBF). Measurements at HIT were financed from the HITRIplus grant (agreement No 101008548) of EU Horizon2020. Parts of the experimental setup were financed from the program "Excellence Initiative – Research University" at the Jagiellonian University (Research Support Module No. U1U/W17/NO/28). When working on the project, Jorge Roser was partially supported from the DFG Grant COMMA, project number 383681334. The authors are responsible for the content of this publication.

References

- [1] Proton Therapy Co-Operative Group. <https://www.ptcog.site/>, Accessed: 2024-10-21.
- [2] “NuPECC report 2014: Nuclear Physics for Medicine”. <http://www.nupecc.org/pub/npmed2014.pdf>. Accessed: 2021-07-13.
- [3] C.-H. Min *et al.* “Prompt gamma measurements for locating the dose falloff region in the proton therapy”. *Applied Physics Letters*, **89(18)** (2006). doi:10.1063/1.2378561.
- [4] J. M. Verburg and J. Seco. “Proton range verification through prompt gamma-ray spectroscopy”. *Physics in Medicine and Biology*, **59(23)**, 7089 (2014). doi:10.1088/0031-9155/59/23/7089.
- [5] M. Pinto *et al.* “Absolute prompt-gamma yield measurements for ion beam therapy monitoring”. *Physics in Medicine and Biology*, **60(2)**, 565 (2015). doi:10.1088/0031-9155/60/2/565.
- [6] L. Kelleter *et al.* “Spectroscopic study of prompt-gamma emission for range verification in proton therapy”. *Physica Medica*, **34**, 7 (2017). doi:10.1016/j.ejmp.2017.01.003.
- [7] M. Pinto. “Prompt-gamma imaging in particle therapy” (2024). doi:10.1140/epjp/s13360-024-05664-4.

- [8] C. Richter *et al.* “First clinical application of a prompt gamma based in vivo proton range verification system”. *Radiotherapy and Oncology*, **118(2)**, 232 (2016). doi:10.1016/j.radonc.2016.01.004.
- [9] J. Berthold *et al.* “First-in-human validation of CT-based proton range prediction using prompt gamma imaging in prostate cancer treatments”. *International Journal of Radiation Oncology Biology Physics*, **111**, 1033 (2021). doi:10.1016/j.ijrobp.2021.06.036.
- [10] S. Bertschi *et al.* “Potential margin reduction in prostate cancer proton therapy with prompt gamma imaging for online treatment verification”. *Physics and Imaging in Radiation Oncology*, **26** (2023). doi:10.1016/j.phro.2023.100447.
- [11] Y. Xie *et al.* “Prompt gamma imaging for in vivo range verification of pencil beam scanning proton therapy”. *International Journal of Radiation Oncology, Biology, Physics*, **99(1)** (2017). doi:10.1016/j.ijrobp.2017.04.027.
- [12] M. Pinto *et al.* “Design optimisation of a tof-based collimated camera prototype for online hadrontherapy monitoring”. *Physics in Medicine and Biology*, **59**, 7653 (2014). doi:10.1088/0031-9155/59/24/7653.
- [13] J. H. Park *et al.* “Multi-slit prompt-gamma camera for locating of distal dose falloff in proton therapy”. *Nuclear Engineering and Technology*, **51(5)**, 1406 (2019). doi:10.1016/j.net.2019.03.008.
- [14] B. F. Huisman *et al.* “Analytical modeling and Monte Carlo simulations of multi-parallel slit and knife-edge slit prompt gamma cameras”. *Physics in Medicine and Biology*, **68** (2023). doi:10.1088/1361-6560/acd237.
- [15] Y. Ku *et al.* “Tackling range uncertainty in proton therapy: Development and evaluation of a new multi-slit prompt-gamma camera (mispge) system”. *Nuclear Engineering and Technology*, **55**, 3140 (2023). doi:10.1016/j.net.2023.05.028.
- [16] J. Ready *et al.* “MO-FG-CAMPUS-JeP1-01: Prompt Gamma Imaging with a Multi-Knife-Edge Slit Collimator: Evaluation for Use in Proton Beam Range Verification”. *Medical Physics*, **43(6)**, 3717 (2016). doi:10.1118/1.4957338.
- [17] J. F. Ready. *Development of a multi-knife-edge slit collimator for prompt gamma ray imaging during proton beam cancer therapy*. PhD thesis, University of California, Berkeley (2016). <http://adsabs.harvard.edu/abs/2016PhDT.....151R>.
- [18] W. Lu *et al.* “Simulation Study of a 3-D Multislit Prompt Gamma Imaging System for Proton Therapy Monitoring”. *IEEE Transactions on Radiation and Plasma Medical Sciences*, **6**, 355 (2022). doi:10.1109/TRPMS.2021.3107411.
- [19] M. J. Cieślak, K. A. Gamage, and R. Glover. “Coded-aperture imaging systems: Past, present and future development – a review”. *Radiation Measurements*, **92**, 59 (2016). doi:10.1016/j.radmeas.2016.08.002.

- [20] E. E. Fenimore and T. M. Cannon. “Coded aperture imaging with uniformly redundant arrays”. *Applied Optics*, **17**, 337 (1978). doi:10.1364/AO.17.000337.
- [21] S. R. Gottesman and E. E. Fenimore. “New family of binary arrays for coded aperture imaging”. *Applied Optics*, **28**, 4344 (1989). doi:10.1364/ao.28.004344.
- [22] J. G. Ables. “Fourier transform photography: A new method for x-ray astronomy”. *Publications of the Astronomical Society of Australia*, **1**, 172 (1968). doi:10.1017/S1323358000011292.
- [23] R. H. Dicke. “Scatter-hole cameras for x-rays and gamma rays”. *ApJL*, **153**, L101 (1968). doi:10.1086/180230.
- [24] S. Sun, Y. Liu, and X. Ouyang. “Near-field high-resolution coded aperture gamma-ray imaging with separable masks”. *Nuclear Instruments and Methods in Physics Research Section A: Accelerators, Spectrometers, Detectors and Associated Equipment*, **951**, 163001 (2020). doi:10.1016/j.nima.2019.163001.
- [25] R. Hetzel *et al.* “Near-field coded-mask technique and its potential for proton therapy monitoring”. *Physics in Medicine and Biology*, **68**, 245028 (2023). doi:10.1088/1361-6560/ad05b2.
- [26] J. Kasper *et al.* “The SiFi-CC project – Feasibility study of a scintillation-fiber-based Compton camera for proton therapy monitoring”. *Physica Medica*, **76**, 317 (2020). doi:10.1016/j.ejmp.2020.07.013.
- [27] J. Roser *et al.* “Range monitoring capabilities with the sifi-cc detector: Spectral-spatial imaging with monte carlo-simulated data”. *Acta Physica Polonica B Proceedings Supplement*, **17**, 1 (2024). doi:10.5506/APhysPolBSupp.17.7-A9.
- [28] K. Rusiecka. *The SiFi-CC detector for beam range monitoring in proton therapy - characterization of components and a prototype detector module*. PhD thesis, Jagiellonian University, Kraków, Poland (2023). doi:10.48550/arXiv.2306.10820.
- [29] K. Rusiecka *et al.* “A systematic study of LYSO:Ce, LuAG:Ce and GAGG:Ce scintillating fibers properties”. *Journal of Instrumentation*, **16(11)**, P11006 (2021). doi:10.1088/1748-0221/16/11/P11006.
- [30] Taiwan Applied Crystal webpage. <https://www.tacrystal.com/>.
- [31] Broadcom AFBR-S4N44P164M Data sheet. <https://docs.broadcom.com/doc/AFBR-S4N44P164M-DS-4x4-NUV-MT-Silicon-Photo-Multiplier-Array>.
- [32] D. Lo Presti *et al.* “Offset: Optical fiber folded scintillating extended tracker”. *Nuclear Instruments and Methods in Physics Research Section A: Accelerators, Spectrometers, Detectors and Associated Equipment*, **737**, 195 (2014). doi:10.1016/j.nima.2013.11.049.

- [33] Data sheet of ELASTOSIL RT 604, WACKER. <https://www.wacker.com/h/en-gb/medias/ELASTOSIL-RT-604-AB-en-2024.06.16.pdf>.
- [34] A. Di Francesco *et al.* “TOFPET 2: A high-performance circuit for PET time-of-flight”. *Nuclear Instruments and Methods in Physics Research Section A: Accelerators, Spectrometers, Detectors and Associated Equipment*, **824**, 194 (2016). doi:10.1016/j.nima.2015.11.036.
- [35] PETsys. “SiPM Readout System” (2023). https://www.petsyselectronics.com/web/website/docs/products/product4/Long%20Flyer%20SiPM%20readout%20chain_v15.pdf.
- [36] M. Wong *et al.* “Comparison of readout systems for high-rate silicon photomultiplier applications”. *Journal of Instrumentation*, **19**, P01019 (2024). doi:10.1088/1748-0221/19/01/P01019.
- [37] NIST. “X-Ray Mass Attenuation Coefficients”. <https://physics.nist.gov/PhysRefData/XrayMassCoef/ElemTab/z74.html>.
- [38] P. Anfré *et al.* “Evaluation of fiber-shaped lyso for double readout gamma photon detection”. *IEEE Transactions on Nuclear Science*, **54**, 391 (2007). doi:10.1109/TNS.2007.892942.
- [39] NIST. “Stopping-power and range tables for protons”. <https://physics.nist.gov/PhysRefData/Star/Text/PSTAR-t.html>.
- [40] S. Agostinelli *et al.* “Geant4—a simulation toolkit”. *Nuclear Instruments and Methods in Physics Research Section A: Accelerators, Spectrometers, Detectors and Associated Equipment*, **506(3)**, 250 (2003). doi:10.1016/S0168-9002(03)01368-8.
- [41] “Geant4: Physics List Guide”. <https://geant4-userdoc.web.cern.ch/UsersGuides/PhysicsListGuide/fo/PhysicsListGuide.pdf>. Accessed: 2024-10-29.
- [42] A. Wrońska *et al.* “Prompt-gamma emission in geant4 revisited and confronted with experiment”. *Physica Medica*, **88**, 250 (2021). doi:https://doi.org/10.1016/j.ejmp.2021.07.018.
- [43] E. Dietz-Laursonn *et al.* “Goddess: A geant4 extension for easy modelling of optical detector components”. *Journal of Instrumentation*, **12**, P04026 (2017). doi:10.1088/1748-0221/12/04/P04026.
- [44] P. Electronics. “TOFPET2 ASIC SiPM Readout System - Software User Guide” (2024). <https://www.petsyselectronics.com/web/website/documentation/TOFPET2%20Downloads/Documentation/PETsys%20TOFPET%20%20ASIC%20SiPM%20Readout%20System%20-%20Software%20User%20Guide%20v2024.08.pdf>.
- [45] R. Brun and F. Rademakers. “Root — an object oriented data analysis framework”. *Nuclear Instruments and Methods in Physics Research Section A: Accelerators, Spectrometers, Detectors and Associated Equipment*, **389(1)**, 81 (1997). doi:10.1016/S0168-9002(97)00048-X.

- [46] SiFi-CC. “sifi-framework. A data analysis software”. https://github.com/SiFi-CC/sifi-framework/tree/4to1_classes_HIT_refactoring.
- [47] L. A. Shepp and Y. Vardi. “Maximum likelihood reconstruction for emission tomography”. *IEEE Transactions on Medical Imaging*, **1(2)**, 113–122 (1982). doi:10.1109/tmi.1982.4307558.
- [48] K. Lange and R. Carson. “Em reconstruction algorithms for emission and transmission tomography”. *IEEE Transactions on Medical Imaging*, **8(2)**, 306 (1984).
- [49] P. Gueth *et al.* “Machine learning-based patient specific prompt-gamma dose monitoring in proton therapy”. *Physics in Medicine and Biology*, **58(13)**, 4563–4577 (2013). doi:10.1088/0031-9155/58/13/4563.
- [50] P. Electronics. “TOFPET2: a high-performance ASIC for time and amplitude measurements of SiPM signals in time-of-flight applications”. https://www.petsyselectronics.com/web/website/docs/products/product1/TOFPET2_Overview.pdf.
- [51] S. Sun, Y. Liu, and X. Ouyang. “Design and performance evaluation of a coded aperture imaging system for real-time prompt gamma-ray monitoring during proton therapy”. *Radiation Physics and Chemistry*, **174** (2020). doi:10.1016/j.radphyschem.2020.108891.
- [52] M. Pinto *et al.* “Design optimisation of a TOF-based collimated camera prototype for online hadrontherapy monitoring”. *Physics in Medicine and Biology*, **59(24)**, 7653 (2014). doi:10.1088/0031-9155/59/24/7653.